1 # SEITCOM-1D: An Interactive 1D Code for temperature and
2 # composition modelling of the crust and mantle from seismological
3 # data

4

5 Mariano S. Arnaiz-Rodríguez [1*,2], Javier Fullea [1,3]

6 [1] Department of Physics of the Earth and Astrophysics, Universidad Complutense de Madrid (UCM). Madrid 28040,

7 Spain.

8 [2] Institut de Physique du Globe de Paris, Université de Paris UMR 7154, CNRS, F-75005 Paris, France

9 [3] Geophysics section, Dublin Institute for Advanced Studies, Dublin, Ireland

10 *Correspondence to*: Mariano S. Arnaiz-Rodríguez (mararnai@ucm.es)

11 Contact: Mariano S. Arnaiz-Rodríguez (mararnai@ucm.es)

12 **Abstract:** We present SEITCOM-1D, a software to model the Earth's thermochemical and geophysical structure from
13 the surface down to the core-mantle boundary (CMB). The code is designed to estimate geophysical parameters of the
14 Earth's crust and mantle from petrological and thermal information within a thermodynamically consistent framework
15 and to perform forward 1D coupled geophysical-petrological modelling of the structure of the Earth. Developed in Julia
16 Language, the open-source code is intended to be an easy-to-use, flexible, and fast. SEITCOM-1D includes tools to
17 exploit the large repertoire of 1D seismological data available, namely: surface wave dispersion curves (of fundamental
18 and higher modes of Rayleigh and Love waves) and receiver functions (of P, S, and SKS waves). Surface heat flow and
19 isostatic topography can also be modelled. Four simple examples that illustrate the capabilities of the code are presented
20 to show the sensitivity of Rayleigh wave phase velocity curves and P-to-S receiver functions to compositional and
21 temperature variations.

22

23

24

25

26

27

28

29

30

31

1 Introduction

33 The interpretation of geophysical data is a complex process that involves the quantitative treatment of measurements in

34 order to retrieve information (presented as models or images) describing the Earth's inner structure (e.g., Aki et al., 1977;

35 Dziewonski and Anderson, 1981; Telford et al., 1990; Grand, 2002; Rawlinson and Sambridge, 2003; Shapiro et al.,

36 2005; Schaeffer and Lebedev, 2013; Fullea et al., 2021). The complexity and reliability of any geophysical model depend

37 extensively on the nature (and quality) of the data selected for its characterization (e.g., Mosegaard & Tarantola, 1997;

38 Bosch, 1999). For example, single-station P-to-S receiver functions analysis can be used to infer the depth of the Moho

39 discontinuity and the average Vp/Vs relationship for all the crust (e.g., Zhu and Kanamori, 2000; Niu and James, 2002),

40 while surface wave dispersion measurements are suitable to image the shear-wave velocity structure of a region via

41 inversion (e.g., Brune and Dorman, 1963; Yanovskaya et al., 1998; Priestley and McKenzie, 2006; Lebedev et al., 2009).

42 Each one of these examples is largely limited by the sensitivity, resolution, and noise inherent to every individual data

43 type. Receiver functions are sensitive to the depth of sharp acoustic interfaces (but can only resolve velocity contrast and

44 not absolute velocities), whereas surface waves are sensitive to shear wave velocity gradients (with comparatively smaller

45 sensitivity to interfaces, e.g., Julià et al., 2000). In order to overcome their individual limitations, both receiver functions

46 and surface waves can be jointly inverted or modeled to study the lithospheric structure under a single seismological

47 station (e.g., Julià et al., 2000; Tkalčić et al., 2012; Calò et al., 2016; Levin et al., 2023).

48 The integration of different data sets generally requires relationships between all the quantitative variables (physical

49 properties) involved in the various forward problems. On the one hand, some of them can be relatively easily connected,

50 like crustal compressional wave velocity (Vp) and density (ρ), for which several empirical formulas exist based on

51 extensive data bases (e.g., Ludwig et al., 1970; Christensen and Mooney, 1995; Godfrey et al., 1997; Brocher, 2005). On

52 the other hand, other parameters like attenuation (Qp, Qs) or the relationship between shear wave velocity (Vs) and

53 density (ρ) are comparatively more difficult to correlate. Although it is tempting to assume that all properties can be

54 correlated by simple equations (e.g. a simple polynomial formulation c.f. Bosch (1999)) or that some may be discarded

55 (e.g., the assumption of elastic wave propagation), the reality is that it is more accurate to describe them with a probability

56 density function within an integrated framework.

57 One effective approach to overcoming this issue is to estimate the required parameters directly from the

58 petrological composition and the in-situ temperature and pressure conditions. For instance, density (ρ) and wave speeds

59 (Vp and Vs) can be estimated from the rock's composition ($\mathcal{C}$), temperature ($\mathcal{T}$) and pressure ($\mathcal{P}$). Furthermore, as

60 porosity and fluids can have a strong effect on these values at upper crustal levels corrections must be applied (e.g., Athy,

61 1930). Therefore, instead of trying to "guess" what an appropriate value for one master property would be, and then

62 compute all others in relation to it (e.g., Jacobsen et al., 2008; Arnaiz-Rodríguez et al., 2021), it is more advantageous

63 and consistent to estimate all parameters directly from the Temperature-Pressure-Rock Composition triad ($\mathcal{TPC}$). In this

64 way, we turn the "plural geophysical data" problem into the "lithology estimation" one, as named by Bosch (1999). The

65 integrated geophysical-petrological strategy, as shown by many previous works (e.g., Afonso et al., 2008; Fullea et al.,

66 2009; Khan et al., 2009; Munch et al., 2018; Bissig et a., 2021; Munch et al., 2021; Fullea et al., 2021), yields

67 thermochemical results more straightforwardly interpreted into geological terms than classical —purely geophysical—

68 approaches. . Here, we present SEITCOM-1D (SEIsmological Temperature and Composition Modeler-1D), a

69 simple forward code to model the thermal and compositional structure of the crust and mantle down to the core-mantle

70 boundary (CMB) primarily from seismological data, i.e., Rayleigh and Love dispersion curves (group and phase velocity

71 curves) and several types of elastic and isotropic receiver functions (the standard P-to-S as well as S-to-P and SKS-to-P).
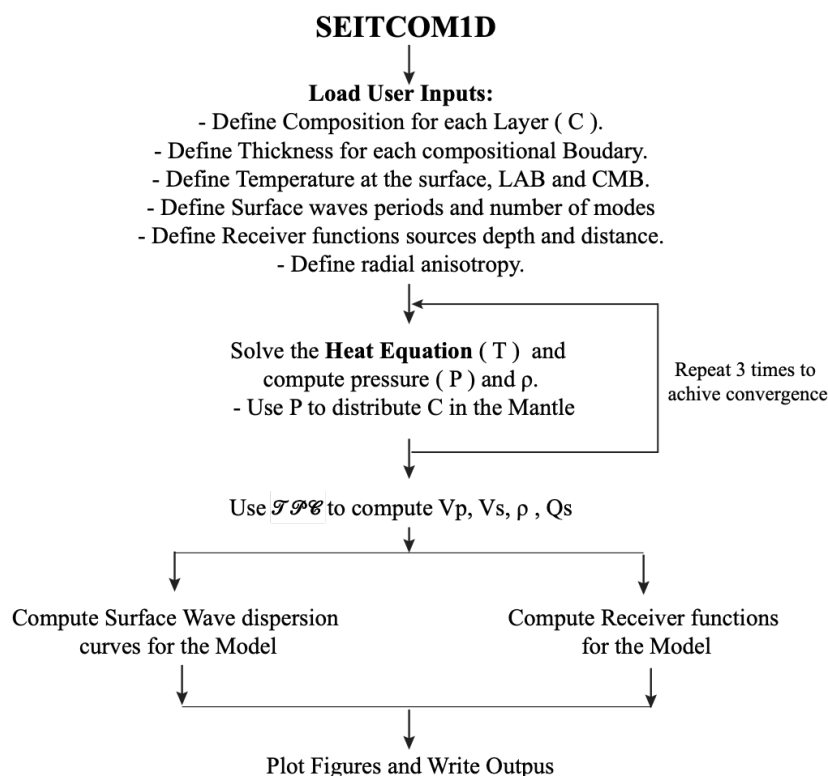
72   Available codes implementing an integrated geophysical-petrological modelling approach (either forward modelling or

73   inversion) are mostly restricted to the lithosphere/upper mantle and do not include a lithological parametrization of the

74   crust (e.g., Afonso et al., 2008, Fullea et al., 2009, Afonso et al., 2013a,b; Fullea et al., 2021).

75   SEITCOM-1D is implemented in Julia Language (Bezanson et al., 2017) for diverse reasons: it is widely used in the

76   scientific community, flexible, open source, efficient, and has cross-platform compatibility, among others. Although Julia

77   is still considered the "new" scientific language, it is actively used in geodesy, geostatistics, and seismology (e.g., Joshua

78   et al., 2020; Xu et al., 2020; Zhu et al., 2022), and it is rapidly spreading across different disciplines (e.g., Dinari et al.,

79   2019; Gao et al., 2020). Among its most notable features are: i) fast execution time (generally approaching C or Fortran-

80   like performance); ii) dynamic typing, debugging, and syntax correction (much like Matlab or Python); iii)

81   interoperability (it makes it easy to integrate codes from C, Python, Fortran, R, Matlab, etc.); iv) geared toward scientific

82   computing; multiple dispatch (multiple methods in the same function for different input arguments); v) powerful parallel

83   computing and GPU capabilities.

84   SEITCOM-1D can be employed to: (a) test geophysical models in the $\mathcal{TPC}$ model space; (b) estimate a possible

85   solution to the composition and thermal structure of the Earth's main layers (limited by the resolution, quality, and

86   sensitivity of the input data), (c) link velocities and density variations to $\mathcal{TPC}$ variations. After introducing the equations

87   and assumptions that drive SEITCOM-1D's engine, the general framework of the code is presented, as well as the

88   validation (against other codes) of the different sections that make up the software package. Finally, a few examples are

89   presented to showcase the functionality and applicability of SEITCOM-1D with a suggestion of additional work for future

90   versions. A general flowchart of the current version of SEITCOM-1D is provided in Fig 1.

91

92

SEITCOM1D

Load User Inputs:
- Define Composition for each Layer (C).
- Define Thickness for each compositional Boudary.
- Define Temperature at the surface, LAB and CMB.
- Define Surface waves periods and number of modes
- Define Receiver functions sources depth and distance.
- Define radial anisotropy.

Solve the **Heat Equation** (T) and
compute pressure (P) and ρ.
- Use P to distribute C in the Mantle

Repeat 3 times to
achive convergence

Use $\mathcal{TPC}$ to compute Vp, Vs, ρ , Qs

Compute Surface Wave dispersion
curves for the Model

Compute Receiver functions
for the Model

Plot Figures and Write Outpus

93

94

95

96 **Figure. 1. SEITCOM1D Flowchart.**

97

98 **2 Methods and Considerations**

99   Mechanical properties of rocks, specifically compressional wave-speed (Vp), shear wave-speed (Vs), and

100 density (ρ), vary in a wide range. Even though there are some clear trends in their behaviour (e.g., sedimentary rocks tend

101 to have lower density than igneous rocks; or mafic rocks have higher Vp than felsic rocks; e.g. Telford et al 1990; Brocher,

102 2005), a large degree of overlap exists. For example, a crustal rock with Vp=6.05 km/s can represent a very old and

103 consolidated carbonatic rock (i.e., a dolomite) or a felsic rock rich in quartz (i.e., a greisen). The consideration of

104 metamorphic rocks affected by, for example, metastability (i.e., departure from thermodynamic equilibrium) makes this

105 statement even more complex, as these rocks tend to show properties different than those associated with its protoliths

106 (e.g., Telford et al., 1990).

107   Seismic velocities and density of Earth's rocks depend on several parameters, namely: temperature, pressure,

108 mineral composition, melt fraction, fluids, and, in the case of crustal rocks, porosity and pore fluids (e.g., Christensen and

109 Mooney, 1995; Brocher, 2005). This complex mixture yields the perfect recipe for the overlap of geophysical parameter

110 values for different rock types and geological settings as usually reported (e.g., Telford et al., 1990; Brocher, 2005). For

111 our purpose of modeling geophysical data using petrological and thermal parameters, it is cardinal to reduce the number

112 of free variables while keeping, at the same time, a flexible enough parameterization to represent the Earth's complexity.

113 In this study, for the crust, we chose several ternary diagrams to classify igneous and sedimentary rocks based on

114 mineralogical composition (Streckeisen, 1974; Le Bas and Streckeisen, 1991; Philpotts and Jay, 2009; Bissell, 2021). By

115 contrast, in the mantle, we adopt two major oxides (Al_2O_3 and FeO) as independent variables and compute the other

116 CFMAS oxides (CaO, FeO, MgO, Al_2O_3, and SiO_2) from statistical correlations based on global mantle xenoliths and

117 peridotite massifs data bases (e.g., Afonso et al., 2013 a,b; Fullea et al., 2021).

118

119 **2.1 The geotherm.**

120 In general, temperature increases with depth (z) within the Earth. Heat transport inside the Earth is mainly a 3D problem

121 in which the mantle is in convection at a high Rayleigh number (Ra > 10^7; e.g., Ricard, 2007), bringing heat from the

122 Core-Mantle Boundary, where the D'' layer acts as the lower hot thermal boundary of the convection, up to the base of

123 the thermal lithosphere, the Lithosphere-Asthenosphere-Boundary (LAB). The LAB (usually defined by the 1250–1330

124 ºC isotherm; e.g., Grose and Afonso, 2019; Ball et al., 2021; Audhkhasi and Singh, 2022) represents the base of the

125 portion of the upper mantle where viscosity is high enough (>1023 Pa s, e.g., Nakada, 1996) to prevent mantle convection,

126 leaving conduction as the dominant heat transport process (e.g., Turcotte et al., 2007). The lithospheric geotherm controls

127 the surface heat flow, which is an output of SEITCOM-1D.

128 Here we are interested in a parametrization that reflects the temperature domain division between the lithosphere and the

129 sublithospheric (upper and lower) mantle, ensuring energy budget consistency across the two domains and being flexible

130 enough to model transient and steady-state thermal situations. The geotherm in SEITCOM-1D follows a 1D thermal

131 parametrization, where the temperature varies only with depth (z):

132

133
$$\rho(z)Cp(z)\frac{DT}{dt} = \frac{\partial}{\partial z}\left(k(z,T)\frac{\partial T}{\partial z}\right) + H_r(z) \quad \text{(Eq. 1)}$$

134 where $\rho(z)$ is the density, $Cp(z)$ is the heat capacity, $k(z,T)$ is the thermal conductivity, and $Hr(z)$ is the radiogenic heat

135 production as a functions of depth (e.g., Gerya, 2007).

136   We solve Eq. 1 on an equispaced 1-km vertical grid using the Finite Differences technique with the following initial and
137   boundary conditions:

138   -   The temperature at the surface of the Earth is constant (and defined by the user).

139   -   The temperature at the CMB is constant (and defined by the user).

140   -   The LAB depth and temperature (e.g., 200 km and 1300 ℃) are defined by the user and are set as an inner boundary
141   condition to the solution of Eq.1. This point is fixed in the solution (unless a collocated thermal anomaly is input by
142   the user) and, therefore, it divides the temperature field into two domains: from the surface to the LAB (conductive
143   geotherm, typically 5-25 K/km), and from the LAB to the CMB (convective geotherm, typically 0.25-0.6 K/km).

144   -   The asthenospheric (or sublithospheric mantle, depth > LAB depth), the transitional mantle (or transition zone, i.e.,
145   from 410 km to 660 km depth), and the lower mantle (depth >660 km) geotherms are defined by two initial temperature
146   gradients provided by the user (by default, 0.45 K/km in the asthenosphere and transition zone, and 0.25 K/km in the
147   lower mantle). Therefore, below the lithosphere, a pseudo-convective geotherm is calculated, solving Eq. 1 for the
148   initial conditions from the thermal gradients. In this way, we parametrize a continuous temperature gradient in the
149   thermal buffer immediately below the lithosphere where both conduction and convective processes are expected.

150   -   The time variable in Eq. 1 is, in general, taken large enough to reach thermal steady-state conditions. Transient thermal
151   scenarios in the lithosphere can be modeled by adding the appropriate time input.

152   -   Vertical variations in radiogenic heat production, thermal conductivity, and heat capacity are considered in the
153   temperature modeling within SEITCOM-1D. The thermal conductivity of mantle rocks is computed according to the
154   equation and parameters proposed by Hofmeister (1999) as a function of temperature, pressure, and predominant
155   mineral type. In this work, we assume one representative mineral chosen from the pyrolite compositional model (e.g.,
156   Ringwood, 1982; Irifune and Isshiki, 1998; Irifune et al., 2010; Hirose, 2006) for each mantle section in order to
157   compute thermal conductivity: olivine (lithosphere and asthenosphere), ringwoodite (upper transition zone, from ~410
158   km to ~550 km), wadsleyite (lower transition zone, from ~550 km to ~660 km), and bridgmanite (lower mantle; e.g.,
159   Hamblin and Christiansen, 2004; Lin et al., 2013). The code also offers the possibility of adding thermal anomalies
160   with respect to the conductive (lithosphere) and pseudo-convective geotherm (asthenosphere, transition zone, and
161   lower mantle) computed as described above by setting a depth range and a temperature anomaly.

162

163   Eq. 1 can model the geotherm in a variety of tectonic and geodynamic settings, for example: (a) continental and mature
164   oceanic lithosphere in thermal steady state; (b) Mid Oceanic Ridges and young oceanic lithosphere in transient thermal
165   state; and (c) close to the adiabatic geothermal gradient below the lithosphere with the typical steep increase in
166   temperature observed in the vicinity of the CMB.

167

168   Note that we do not intend to solve a full geodynamic problem in the sublithospheric mantle (i.e., incorporating mantle
169   flow and dynamic topography); instead, we aim for a flexible 1D parameterization able to describe variations in the
170   geothermal gradient or temperature anomalies with respect to the reference geothermal gradients (e.g., plumes or slabs;
171   see Section 4.2 for an example) as imaged by seismic data.

172

173   **2.2 Compositional model space**

174   To simplify the existing plethora of mineral aggregates (rocks), we have split the model compositional space ($\mathcal{C}$) into
175   three major categories: sedimentary rocks, igneous rocks, and mantle rocks. Out of these, only igneous rocks are further
176   separated into three compositional subcategories: felsic, mafic, and ultramafic rocks (after standard geologic

177   classification, e.g., Streckeisen, 1974). In this section, we describe how each rock type is parametrized and how the

178   relevant geophysical parameters are computed from the $\boldsymbol{TPC}$ triad. Metamorphic rocks have been left out of our model

179   parametrization as their mineralogy tends to be complex, as well as some physical features that require complex numerical

180   representation (e.g., distinctive and pronounced planes of weakness). Furthermore, their classification is usually based on

181   texture and not composition, which makes it difficult to relate to our proposed parametrization. Therefore, we favor the

182   use of their protoliths, which are much simpler to describe in terms of their mineral composition and properties. For

183   example, a marble, composed of recrystallized carbonatitic minerals, can be represented as a 0% porosity carbonate. This

184   is a novel scheme as no rigorous thermochemical/lithological parametrization has been presented in previous tools

185   designed for integrated modelling of the lithosphere (e.g., Afonso et al., 2008, 2013a, b; Fullea et al., 2009, 2021).

186

187

188   **2.2.1 Sedimentary Rocks**

189   In SEITCOM-1D the sedimentary compositional space ($\boldsymbol{C}$) is discretized following the simplest ternary diagram

190   provided by Bissell (2021). Based on it, each corner of the ternary diagram stands for:

191   -   α-Quartz (Qz).

192   -   Carbonates: represented in our model by pure calcite ($CaCO_3$) as it is much more common than dolomite

193   ($CaMg(CO_3)_2$)

194   -   Clay Minerals ($[Al, Fe]_2O_3$): representing a *mélange à parts égales* (from here onwards, màpé) of three commonly

195   occurring clay minerals: Montmorillonite + Kaolinite + Illite.

196   We use the code MinVel (Hacker et al., 2004; Abers et al., 2016; Sowers et al., 2019), an extensive database of physical

197   properties of minerals from laboratory measurements (Haker et al., 2003), to estimate Vp, Vs, and ρ for all the

198   compositional space ($\boldsymbol{C}$), defined by the possible combinations of the minerals (3 values that add up to 100%, e.g., 60 %

199   quartz + 20% carbonates + 20 % clays) every 10%, for different temperatures (between 200 and 1000 K every 100 K)

200   and pressures (between 0 and 0.6 GPa every 0.025 GPa). This sampling yields three multidimensional grids (one for each

201   property) in which rock properties are stored for a range of $\boldsymbol{TPC}$ values. These are linearly interpolated and saved into

202   easy-to-call Julia functions. In this way, we can estimate Vp, Vs and ρ for a fully consolidated sedimentary unit from any

203   given $\boldsymbol{TPC}$ values (compositions are limited to triads consisting of multiples of 10 to guarantee numerical precision and

204   computational speed). Fig. 2 presents several examples of the geophysical properties in ternary diagrams. Notice that

205   carbonatic rocks tend to show larger velocity and density values than other lithologies, regardless of temperature, pressure

206   conditions, or porosity, and clays show the largest variations.

207

208   **2.2.1.1 Porosity**

209   Crustal rocks are not perfect aggregates of minerals, and their behavior is not completely elastic in some cases.

210   Sedimentary rocks are generally porous, and hence we correct their geophysical properties by the percentage of porosity

211   (φ). Velocities (Vx) are corrected in accordance with Raymer's equations (Raymer et al., 1980), while density (ρ) is

212   corrected following Athys's law (Athy, 1930):

213

214    $$V_{rock} = (1 - \varphi/100)^2 V_{solid} + (\varphi/100)V_{liquid} \text{ (Eq. 2)}$$

215    $$\rho_{rock} = (\varphi/100 - 1)\rho_{solid} \text{ (Eq. 3)}$$

216

217 Where X_{rock} refers to the corrected property, X_{solid} to the property of the fully consolidated rock and X_{liquid} to property of

218 the fluid inside the porous scape. The user must input X_{liquid} of the fluid inside the porous space, if not the corrections are

219 applied by default as if the rocks were filled with air.

220

221 **2.2.2 Crustal Igneous Rocks**

222 For crustal igneous rocks, we use a similar approach to that presented for sedimentary rocks in the previous section,

223 including the use of màpé where required and linear interpolation. In this case, three compositional subspaces are

224 considered, one for each igneous rock subcategory: felsic, mafic and ultramafic rocks (as defined by Streckeisen, 1974;

225 Le Bas and Streckeisen, 1991; Philpotts and Jay, 2009). We treat each subcategory as follows:

226 - Felsic rocks are defined in a ternary space outlined by the QAP diagram (quartz, K-feldespars, and plagioclase). We

227   discard the standard QAFP classification (quartz, K-feldespars, feldesphatoids, and plagioclase) in favor of a 3-mineral

228   space as feldspathoids (F) resemble feldspars (K), and rocks with high concentrations of F are comparatively much

229   less common. Hence, felsic rocks are defined by the ternary of: α-quartz or β-quartz (as we account for the reversible

230   change at 573 °C, which drastically impacts the determination of Vp, Vs, and ρ; Abers and Hacker, 2016); K-feldespars

231   (a màpé of Orthoclase + Sanidine); and Plagioclase (a màpé of High Albite + Low Albite + Anorthite).

232 - Mafic rocks are considered aggregates of: anorthosite (màpé of Anorthite+High Albite+Low Albite), clinopyroxene

233   (màpé of Diopside+Hedenbergite) and ortopyroxene (màpé of Enstatite+Ferrosilite).

234 - Ultramafic rocks are defined as a combination of olivine (màpé of Forsterite+Fayalite), clinopyroxene (màpé of

235   Diopside+Hedenbergite) and orthopyroxene (màpé of Enstatite+Ferrosilite).

236

237 As with sedimentary rocks, we sample each compositional space with MinVel (Hacker et al., 2004; Abers et al., 2016;

238 Sowers et al., 2019) at variations in composition every 10% for different crustal temperatures (between 0 and 1600 K

239 every 100 K) and pressures (between 0 and 4 GaP every 0.05 GPa) and then save all results into Julia functions. In order

240 to show the variations of the Vp, Vs, and ρ values in a ternary diagram, Fig. 2 presents several examples.

241

242 Typical igneous rocks have very low primary porosity (e.g., 0.05%–0.90% for granite and 0.6–1.3 for basalts, Wieczysty,

243 1982) when compared to sediments (e.g., a typical sandstone has a porosity ranging from 10% to 40%) and are usually

244 found at high $\mathcal{P}$ in the crust. Furthermore, even though crustal rocks are well known to have secondary porosity (e.g. high

245 density faulting), there is no simple way to account for it in Vp,Vs or ρ. Therefore, we choose not to apply any porosity
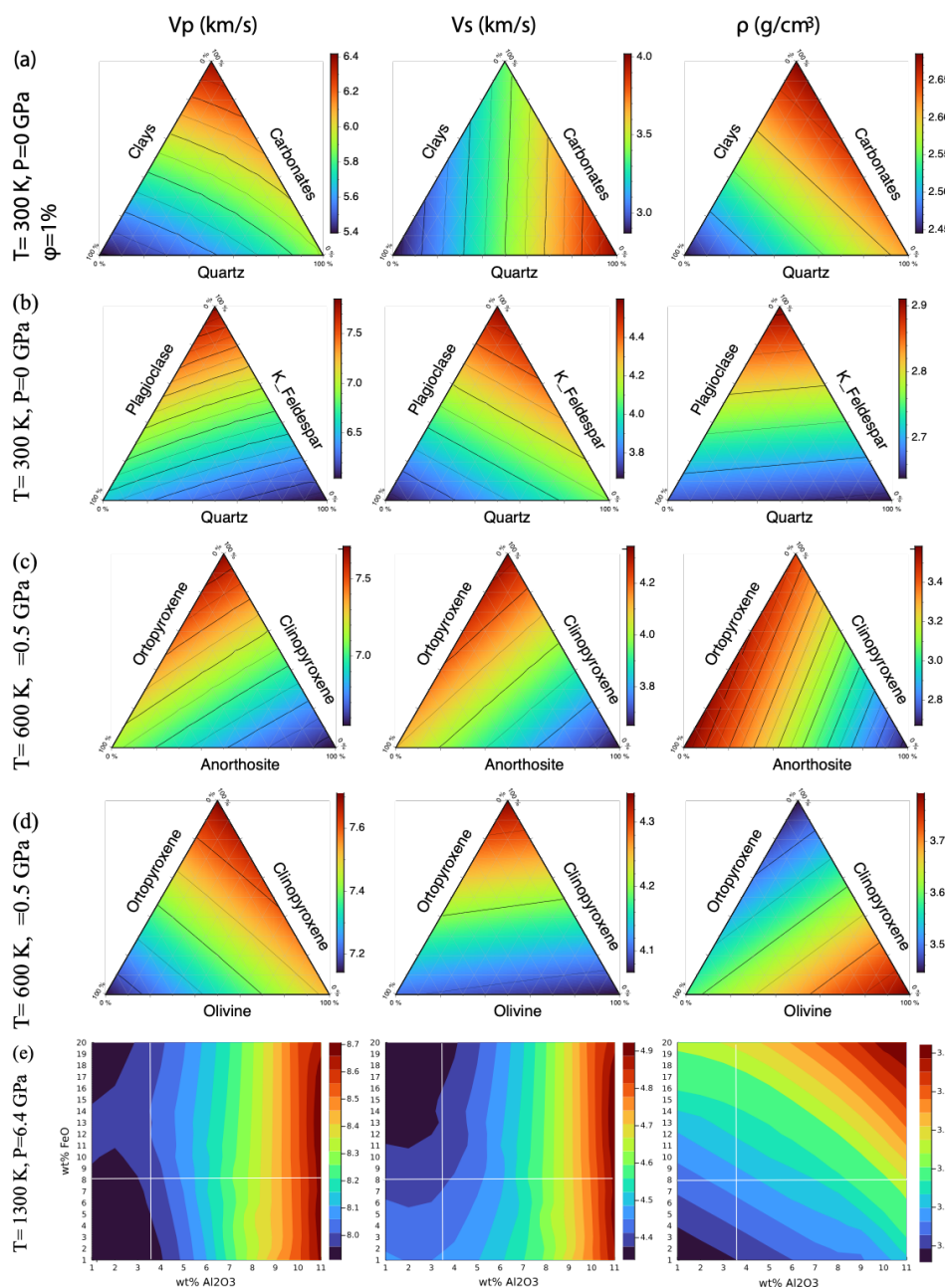
246 corrections for igneous rocks in SEITCOM-1D.

247

248

249

250

251

Figure 2: Examples of compressional wavespeed (Vp), shear wavespeed (Vs) and density (ρ) variations for: (a) sedimentray, (b) igneous felsic, (c) igneous mafic, (d) igneous ultramafic and (e) mantle rocks as a function of temperature (T), pressure (P), composition and porosity (for sedimentary rocks). All color scales are similar for ease of comparison. In sedimentary rocks (a) carbonatics have the higher Vp and ρ. For felsic rocks, with higher percentage of quartz, Vp and ρ becomes higher, while Vs becomes higher with the increase of plagioclase. Also, lower values of all three properties are associated with higher percentage of K-feldspars. For mafic rocks, all properties increase with the percentage of anorthosite and decrese with the percentage of clinopyroxene. Unlike felsic or mafic rocks, in ultramafics, each mineral dominates the decrease of a different property. On (e) the cross marks the average mantle composition.

2.2.3 Mantle Rocks

Compared to the crust, the Earth's mantle petrology is less complex and can be adequately represented by the modal distribution of the main mineral phases (olivine, pyroxenes, and Al-bearing phase) under the consideration of thermodynamic equilibrium (T> 500 °C). In this work we determine stable mantle mineral assemblages using a Gibbs free energy minimization scheme (Connolly, 2005, 2009). Therefore, the mantle's physical properties relevant to our work (Vp, Vs and ρ) are computed on these assumptions based on the $\boldsymbol{TPC}$ values. A standard characterization of mantle composition is based on the main major oxides in the CFMAS system (CaO–FeO–MgO–Al$_2$O$_3$–SiO$_2$; e.g. Irifune, 1990; Irifune and Tsuchiya, 2015). To simplify the parametrization of $\boldsymbol{C}$, here we adopt the discretization of Fullea et al. (2021)

were the wt% amounts Al$_2$O$_3$ and FeO oxides in the mantle layers are free variables, and CaO–MgO amounts are statistically correlated to Al$_2$O$_3$ based on global petrological data bases as described in Afonso et al. (2013a). Similarly to Mg# (= MgO/[MgO + FeO]), Al$_2$O$_3$ has been shown to be a strong compositional indicator and, therefore, an overall proxy for mantle fertility. In contrast, neither FeO nor SiO are correlated in general with either CaO or Al$_2$O$_3$ (Afonso et al. 2013a). For the petrological calculations we use Perple_X (Connolly, 2005, 2009) and for the lower mantle the dababases by Xu et al. (2008) and Stixrude & Litgow-Bertelloni 2021). We sample the wide range of $\boldsymbol{T}$ (from 100 to 4500 K) and $\boldsymbol{P}$ (from 0 to 145 GPa) found in the mantle. As for the self-consistent thermodynamic data base, in the upper mantle we use the Xu et al., (2008), whereas in the transition zone and lower mantle we consider Stixrude & Litgow-Bertelloni (2021). $\boldsymbol{C}$ values are limited to the ranges of (1-11) wt% for Al$_2$O$_3$ and (1-20) wt% for FeO. These range of compositions should be more than enough to model almost every scenario in the entire mantle as values of Al$_2$O$_3$ are expected to range from 1.0 wt% to 6.0 wt% and FeO is generally considered to be around 8.0 wt% (e.g., McDonough and Sun, 1995). In some special cases larger ranges might be needed, e.g., Large Low Shear Velocity Provinces in the lowermost mantle (e.g., Vilella et al., 2021). In Fig. 2 we show the relevant mantle properties for several $\boldsymbol{TP}$ conditions. In SEITCOM-1D, there are four major mantle layers defined by their wt% amounts of Al$_2$O$_3$ and FeO:

1) The *lithospheric mantle* extends from the Moho down to the Lithosphere-Asthenosphere Boundary, or LAB (an input depth and temperature are expected from the user as explained in Section 2.2). The thickness of this layer is user-defined and does not change unless thermal anomalies are incorporated into the model.

2) The *asthenospheric (or sublithospheric) mantle* extends from the LAB down to a pressure of ~14 GPa, representing the average value for the transition from olivine to wadsleyite mineral phases.

3) The *transition zone mantle* extends from a pressure of ~14 GPa to a value of ~24 GPa. The later value is the average pressure for the transition from ringwoodite and majorite to perovskite and ferropericlase, the boundary between the upper and the lower mantle. Note that the transition zone includes an inner phase transition from wadsleyite to ringwoodite at around 520 km depth (Rigden et al., 1991; Tian et al., 2020).

4) The *lower mantle* extends from a pressure of ~24 GPa down to the CMB (a user input).

While the boundaries between the first two layers (i.e., LAB depth) and the bottom of the model (i.e., CMB) are input parameters, in the case of the top and bottom of the mantle transition zone, the depth depends on different mineral phase transitions that cannot be predicted beforehand without performing a thermodynamic calculation based on the actual $\boldsymbol{TPC}$ conditions. Therefore, our approach here is to initially define those mantle layer boundaries based on standard reference pressure values (~14 GPa and ~24 Ga), and subsequently relocate them automatically to the depth at which the relevant phase transitions occur. Therefore, from a compositional point of view, the depth of the base of layer 2 and 3 is effectively defined by a thermodynamic equilibrium calculation. In virtue of the thermodynamic parametrization, the velocity and density jumps related to phase transitions usually associated with the 410 km, 520 km, and 660 km discontinuities will arise in the model even if the composition is uniform across all four mantle layers. For example, all these discontinuities

304   still appear in the model for a constant whole mantle composition (e.g., primitive mantle composition with 3.6 wt% Al2O3

305   and2O3 8.0 wt% FeO from McDonough and Sun, 1995). Finally, the user can also specify anomalous regions

306   (compositional anomalies) within any of the four compositional layers by setting a depth range and a chemical anomaly

307   value (e.g., -0.5 wt% Al2O3 and +0.2 wt% FeO).

308

309   **2.2.3.1 Seismic attenuation in the mantle**

310   To account for anelasticity, we follow the strategy of Dannberg et al. (2017) and extrapolate the relationships for olivine

311   at upper mantle conditions derived by Jackson and Faul (2010) to the whole mantle. Notice that this is clearly a

312   simplification of the mineralogy at the mantle scale and thus its behavior in seismic attenuation terms, but Dannberg et

313   al. (2017) proved that it yields a useful first-order approximation as the results are not very dissimilar to, for example, the

314   values reported in the PREM model. Here we adopt the parametrization by Dannberg et al. (2017) as described in

315   Appendix B.

316

317   Most of the attenuation parameters are different for each major mantle mineral phase. In SEITCOM-1D, we use different

318   attenuation parameters for the most abundant mineral phases at each depth depending on their respective stability fields:

319   the upper mantle (olivine), the upper and lower transition zones (wadsleyite and ringwoodite), and the lower mantle

320   (perovskite). Grain size (d) has a large impact on the attenuation, as per our parametrization described in Appendix B. In

321   the code, the user can choose between three grain size models with depth: (a) a constant value (d = 10 mm), (b) the model

322   by Schierjott et al. (2020), in which d increases with depth, and (c) the model by Dannberg et al. (2017), where d decreases

323   with depth. In general terms, we find that the constant and Schierjott models fit best with the general trends of the global
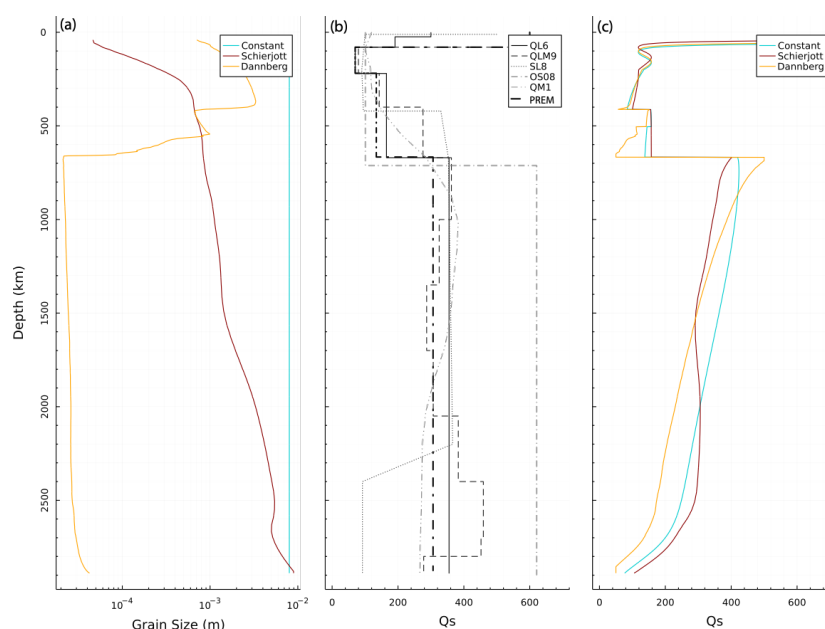
324   1D models (Fig. 3).

325

328   **Figure 3: (a) Grain size variation with depth for the 3 models included in the code: Constant (a constant value or 10^-2 m),**
329   **Schierjott (the grain size variations estimated by Schierjott et al., 2020) and Dannberg (the grain size variations estimated by**
330   **Dannberg et al., 2017). (b) Several 1D Radial models of Qs for the whole mantle: SL8 (Anderson and Hart, 1978), QM1**

331   **(Widmer et al., 1991), QL6 (Durek and Ekstrom, 1996), QLM9 (Lawrence and Wysession, 2006), QOS08 (Oki and Shearer,**
332   **2008), PREM (Dziewonski and Anderson, 1981). (c) Qs computed from the Burguers model of of linear viscoelasticity (Jackson**
333   **and Faul, 2010). The Constant and Schierjott models produce the closest fit the radial models.**

334   **2.2.4 Melt**

335   Accounting for melt in a 1D column requires the definition of consistent solidus and liquidus curves for the crust and the

336   whole mantle. In the crust, we consider the equations in Gerya (2019) characterizing the solidus and liquidus temperatures

337   for sediments and igneous rocks. In the mantle, water content and, to a lesser extent, composition control the solidus

338   values reported in the literature (e.g., Schmidt and Poli, 1998; Hirschmann, 2000; Katz et al., 2003; Sarafian et al., 2016;

339   Fu et al., 2018). In SEITCOM-1D, we allow the user to define the solidus curve for the upper mantle (i.e., from the Moho

340   to a pressure of ~ 10 GPa or depth of ~300 km) from two sources:

341   - The solidus presented by Andrault et al. (2018), which corresponds to a nominally dry mantle (between 1 and 90 wt

342   ppm),

343   - The second-degree polynomial by Katz et al. (2003), defined only up to 7 GPa, which corresponds to a nominally

344   anhydrous mantle with 40–80 wt ppm of water.

345

346   From 10 GPa to 30 GPa, we use the logarithmic anhydrous solidus curve by Herzberg et al. (2000), and from 30 GPa to

347   120 GPa, the solidus curve by Fu et al. (2018) with ~ 400 wt ppm water can be extrapolated to the CMB conditions,

348   according to the authors.

349   For the mantle liquidus, we use (a) a fourth-degree polynomial fitted to the liquidus curve by Litasov and Ohtani (2002),

350   valid from 0 GPa (surface) to ~30 GPa (roughly 800 km depth), and (b) a second-degree polynomial fitting the liquidus

351   curve by Fu et al. (2018) from 30 GPa to the CMB. With this parametrization, the solidus and liquidus curves have large

352   jumps at the crust-mantle boundary and around 800 km, therefore we have chosen to smooth them with a rloess (Fig. 11).

353   The volumetric melt fraction (Melt) is usually defined, for a constant pressure, as a linearly varying temperature-

354   dependent function (e.g., Gerya and Yuen, 2003b; Burg and Gerya, 2005; Gerya, 2019; Fullea et al., 2021):

355

356   $$Melt = 0\% \text{ from } T \leq T_{solidus} \text{ (Eq. 4)}$$

357

358   $$Melt = \frac{(T - T_{solidus})}{(T_{liquidus} - T_{solidus})} 100 \text{ from } T_{solidus} < T < T_{liquidus} \text{ (Eq. 5)}$$

359

360   $$Melt = 100\% \text{ at } T \geq T_{liquidus} \text{ (Eq. 6)}$$

361

362   where $T_{solidus}$ and $T_{liquidus}$ are the wet solidus and dry liquidus temperatures defined by the curves described previously.

363   Once *Melt(z)* has been computed for each model node the associated seismic parameters (Vp, Vs, Qs) are corrected

364   following the experimental study by Chantel et al (2016):

365   $$V_P = 0.07 Melt^2 - 0.5566 Melt + 7.9235 \text{ (Eq. 7)}$$

366

367   $$V_S = 0.065 Melt^2 - 0.5565 Melt + 4.4211 \text{ (Eq. 8)}$$
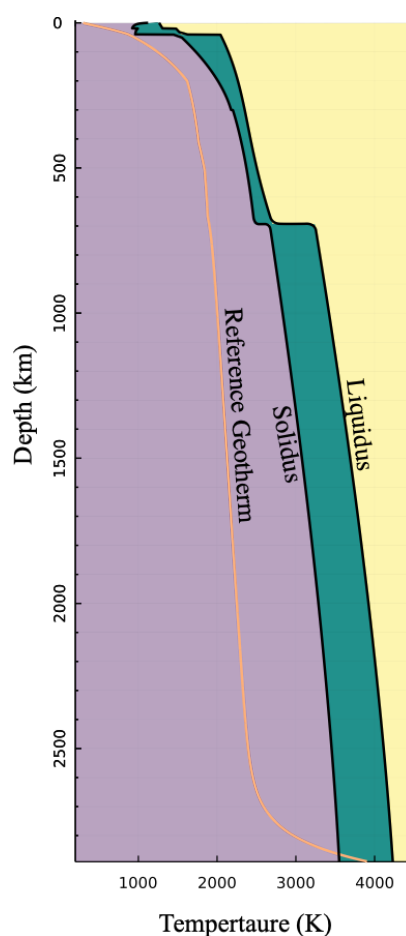
368

369   $$100/Q_S = 2.4063 ln(Melt) + 5.9284 \text{ (Eq. 9)}$$

370

371   Mantle density is corrected (becoming the effective density, ρ_{eff}) by the equation postulated by Gerya (2019):

372    $$\rho_{eff} = \rho_{solid}(1 - Melt + Melt \frac{\rho_{0molten}}{\rho_{0solid}}) \text{ (Eq. 110)}$$

373   where ρ_{0solid} and $\rho_{0liquid}$ are the standard densities of the solid and molten rock, respectively and ρ_{solid} is the density of the

374   solid rock at given $\mathcal{TP}$ conditions computed as described in section 2.1 and 2.3. The values for ρ_{0solid} and $\rho_{0liquid}$ are taken

375   from the compilation of values by Gerya (2019) and could be changed by the user inside the code if required. Figure 4

376   shows the used curves.

377
378
379
380
381
382
383
384
385
386
387
388
389
390
391
392
393
394
395
396
397
398
399
400
401
402
403
404
405
406
407

408   **Figure 4: Solidus and liquidus curves from the entire crust and mantle. Solidus by: Gerya (2019), Katz et al., (2003), Herzberg**
409   **et al (2000) and Fu et al., (2018). Liquidus by: Gerya (2019), Litasov and Ohtani (2002) and Fu et al., (2018). See text for details.**

410
411

412

413

414

415

416 **2.4 Surface Wave Dispersion Forward Modeling**

417 SEITCOM-1D computes surface wave dispersion curves in two ways: from a native function SWD.jl (developed as part

418 of SEITCOM-1D) or by calling Mineos.jl, a Julia wrapper around the code Mineos developed to compute normal modes

419 of the Earth (Master et al., 2011, https://geodynamics.org/cig). In general terms, SWD.jl is faster than Mineos.jl, although

420 the former gives an approximated solution in contrast to the exact solution from the latter. Also, the approximations built

421 in SWD.jl yield some high errors (>1%) in cases of very strong attenuation ($Qs < 70$) and high-order overtone calculation.

422 SWD.jl is mostly based on the formulation described by Haney and Tsai (2015, 2017, 2019). These authors utilize (for

423 both Rayleigh and Love waves) a finite element approach based on the thin-layer method (Lysmer, 1970; Kausel, 2005).

424 The scheme behind SWD.jl and the corrections necessary to approximate the results from Mineos.jl are detailed in

425 Appendix A. To validate both approaches, in Fig. 5, we present a comparison between surface wave dispersion curves

426 computed by SWD.jl (the main SEITCOM-1D dispersion engine), Mineos (Masters et al., 2011) and the exact solution.

427 Each code uses a different approach for the computation: SWD.jl uses a finite element solution, whereas Mineos uses the

428 traditional normal-mode summation. Discrepancies in the results from all three codes are small ($dc < 0.045\%$ and $dU <$

429 0.2%) and might arise from the difference in the computations and/or parameterization of the model for each code. For

430 example, at $T = 50$ s, considering the PREM velocity model as input, the fundamental mode Rayleigh wave phase velocity

431 differences comparing the output of the three codes are $<0.002\%$. Notice that errors increase with time because of the

432 spherical approximation. The user can always extract the standard seismic velocities and density geophysical model from

433 the SEITCOM-1D output to perform customized seismic modeling a posteriori with other tools. We recommend using

434 Mineos.jl for modeling data with long periods ($T > 70$ s), many overtones, and for studying regions with strong

435 attenuation. Note that the original Mineos code has a limitation of 300 velocity layers. On the other hand, SWD.jl is

436 recommended for shorter periods ($T < 100$ s; mainly crust studies) where complex models can be proposed or when

437 computational time is relevant.

438
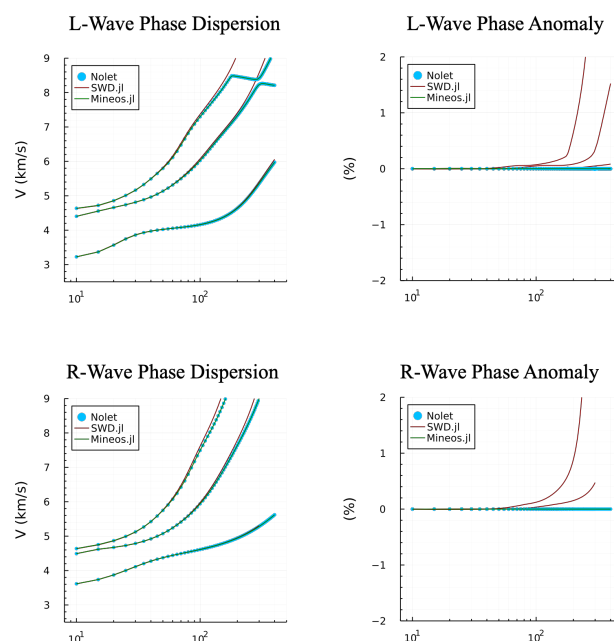
Figure 5: Comparison between surface wave dispersion curves computed by SWD.jl (red, the main SEITCOM-1D dispersion engine), Mineos (green, Masters et al., 2011) and the exact solution (blue circles marked as Nolet).

2.5 Receiver Functions Forward Modeling

In order to give the user a basic handling of receiver function data during the modeling stages, we have incorporated a simple module (i.e., the computation is made without accounting for the effect of anisotropy or attenuation) to compute synthetic receiver functions from the input geophysical model. Receiver functions are computed using a transfer function between the stress and displacement known as the propagator matrix approach (Thomson, 1950; Haskell, 1953; Kennett, 1983). For all the receiver functions, P-to-S, S-to-P, and SKS-to-P, the sequence is similar. For each source (with a depth and epicentral distance taken from the IASPI91 tables; Kennett et al., 1991), the synthetic radial and vertical components (R and Z) are computed for a given 1D model and then rotated into the direction of polarization of the incident P-wave (L) and its perpendicular (Q) in the R-Z plane (e.g., Vinnik, 1977; Kind et al., 1995). In general, we compute the surface response in the Fourier domain for a plane impingement waveform. The transmitted impulse is assumed to arrive at the surface at t = 0 s. Then, we calculate the time domain displacements at the surface for each direction. The computation includes all multiples, transformations, and reflections produced by an arbitrary structure with homogeneous layers (Svenningsen and Jacobsen, 2007). Finally, the Z (or L) component records are deconvolved from the R (or Q) components, and a Gaussian low-pass filter is applied to the resulting seismogram. For the S wave incidence, the resultant seismograms are subject to time and sign reversals, following the convention for S receiver functions (e.g., Yuan et al., 2006). This process is repeated n times (as many RFs are input by the user) for a list of events (epicentral distances and depths). The resulting n receiver functions are stacked via move-out correction considering the IASPI91 model and a reference velocity of 6.4 km/s (e.g., Rondenay, 2009). The final stacked receiver functions are compared with the observed waveforms to measure misfits. Fig. 6 shows a comparison between the results of the RF computations in SEITCOM-1D and those from other codes in order to validate the results.

For these comparisons (and by default in the code), RF are normalized, as amplitude values may vary with instruments and processing. No other corrections are applied to the final stack, and the post-processing (if required) is left to the end

465 user. Furthermore, attenuation and anisotropy effects are not accounted for, the code automatically outputs a geophysical

466 model (z, Vp, Vs, ρ, Qs, χ) that can be used for forward computation and individual RF for post-processing using other

467 modelling tools. It is important to keep in mind that real RF are highly dependent on the quality of the data and the steps

468 used by the interpreter. In general, there are several ways to approach the deconvolution of the horizontal and vertical

469 components of the seismogram that may differ from the scheme presented here (e.g., Pesce, 2010). Here, we use the now-

470 classic implementation of the frequency-domain water-level algorithm (e.g., Langston, 1979; Rondenay, 2009). Hence,

471 when modeling real RF with SEITCOM-1D, care must be taken to consider the aforementioned points for consistency,

472 especially regarding anisotropy and attenuation.

473

474

475

476

477

478

479

480

481

482

483

484

485

486

487
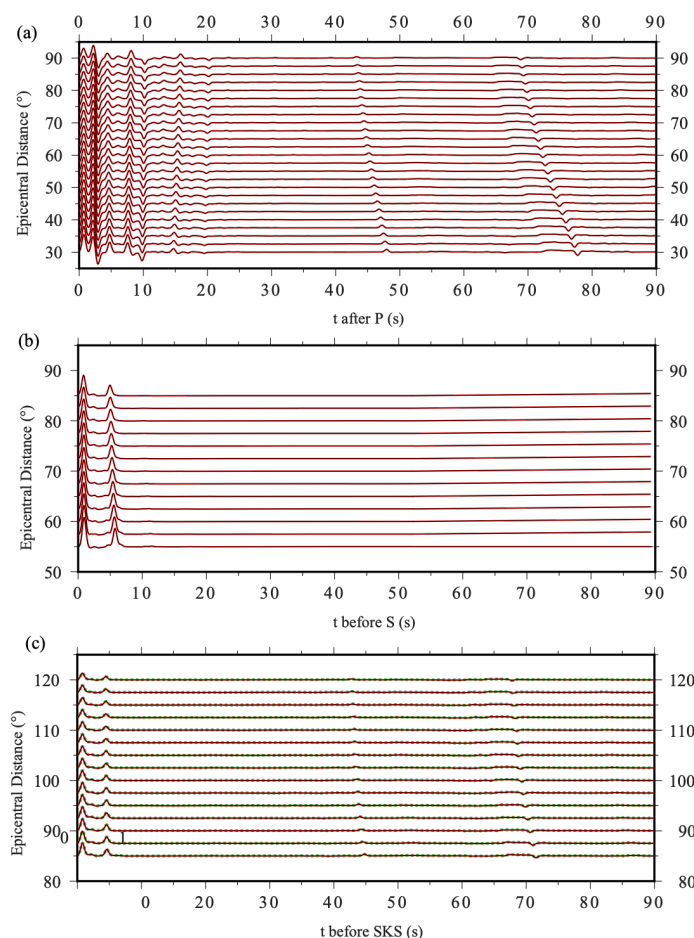
Figure 6: Comparison between the synthetic Receiver Functions (RF) computed by the code and those computed with other codes. (a) P-to-S RF, (b) S-to-P RF and (c) SKS-to-P RF. RF in red correspond to our code, those in black were computed with the Matlab codes by Bo Holm Jacobsen (2008; Svenningsen and Jacobsen, 2007), and on green those computed in IRFFM2 V1.2 (Tkalčić et al, 2012, only P-to-S available). Difference are small (error < 0.1%). For this example the gaussian parameter a = 2.5 (roughly between 0.4 and 1 Hz).

3. Testing SEITCOM-1D: Sensitivity analysis

To illustrate the capabilities of SEITCOM-1D, we present three simple examples that demonstrate the sensitivity of Rayleigh wave phase velocity curves and P-to-S receiver functions to compositional and temperature variations with respect to a reference model (Figure. 14–16). The reference model in our examples is characterized by:

i. A 40-km-thick crust with a 2-km shale sedimentary layer (Qz(%)=30, Carbo(%)=10, Clays(%)=60, Porosity(%)=5), a 20 km thick monzodioritic (felsic) upper crust (Qz(%)=10, K-feldespar(%)=90, Plagioclase(%)=0), and a 20-km thick orthopyroxene-gabbroic (mafic) lower crust (Anorthosite(%)=20, Clinopyroxene(%)=60, Orthopyroxene(%)=20).

ii. A 200-km-thick lithosphere with a LAB temperature of 1300 ºC.

iii. A uniform whole mantle composition: Al2O3=3.6 wt% and FeO=8.0 wt% (e.g., McDonough and Sun, 1995) with constant grain size (10 mm).

iv. Isotropic model (i.e., no radial anisotropy)

3.1 Example 1: Average Mantle Composition

In this first example (Fig. 7), we change the composition of the entire mantle. The values for the two independent oxides in our parametrization (Al2O3 = 3.6 wt% and FeO = 8.0 wt%) correspond to the primitive mantle composition from McDonough and Sun (1995). Here, we explore the effect of changing the value of Al2O3 to 2.0 wt% and to 5.0 wt% (for a constant value of FeO wt%). Then, the effect of changing the values of FeO to 6.0% and 10.0% (for a constant value of Al2O3 wt%). From this simple test, we can draw a few important conclusions:

- The amount of Al2O3 dominates the velocity gradients in the upper mantle, with velocity variations being proportional to Al2O3 content. However, Al2O3 has a limited effect on the lower mantle.

- The amount of FeO dictates the velocity gradients in the lower mantle while having a minor effect in the upper mantle. In general terms, velocity gradients are inversely proportional to the wt% of FeO in the lower mantle. Interestingly FeO has a dramatic effect on the gradient at the top of the D" layer, changing its depth by ~100 km within our test.

- The sharpness and depth of the transition zone boundaries is controlled by mantle composition. Both Al2O3 and FeO appear to have a dramatic effect on the 410 km discontinuity (olivine->wadsleyite) sharpness. By contrast, the 560 km discontinuity (wadsleyite->ringwoodite) and the 660 km discontinuity (ringwoodite+majorite->perovskite+ferrocerase) are mostly affected by FeO and Al2O3 respectively.

We note that within the chemical parametrization in SEITCOM-1D, the amount of CaO and MgO oxides is dependent on the amount of Al2O3 based on statistical correlations from global petrological data bases (Afonso et al., 2013a;). By contrast, the amount of FeO is an independent variable.
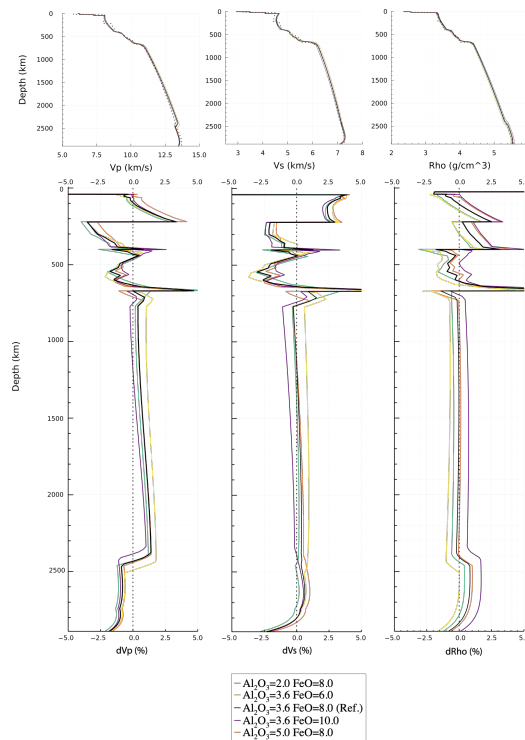
529 **Figure 7: Example 1. Comparison between the results of a constant composition mantle in SEITCOM-1D (solid lines) and the**
530 **PREM model (dashed). Here we have tested several compositions to show how large Vp, Vs and Rho anomalies can arise from**
531 **extreme values of Al2O3 and FeO. Top panels show the comparison in absolute Vp, Vs and Rho values, while the bottom panel**
532 **shows anomalies with respect to PREM . In the bottom panel, crustal anomalies have been deleted from the presentation as**
533 **they are too large as PREM has a poorly estimated crust.**

534 **3.2 Example 2: Cold horizontally stagnating slab**

535 In the second example (Fig. 8), we implement a thermal and compositional anomaly with respect to the reference model

536 representing a 1D section of a cold horizontally stagnating slab (a subducted slab that changes direction in the transition

537 mantle; e.g., Fukao et al., 2009). The anomaly is defined from 300 km to 500 km depth (Fig. 14) and is characterized by:

538 (a) a -600 K thermal anomaly with respect to the ambient mantle; and (b) a chemical anomaly of Al2O3 = -0.25 wt% with

539 respect to our reference model. The mantle in the "slab" region shows higher values for velocities, density, and Qs than

540 the reference model. These positive anomalies are easily recognized in the Rayleigh wave dispersion curves: for the long

541 periods in the fundamental mode and, in general, for the higher dispersion modes, the phase velocity anomalies are >

542 +3%. The P-to-S receiver function is only modified for periods > 20 s (arrival of late phases) due to the upward shift of

543 the 410 km discontinuity caused by the "slab" anomaly.

544

545
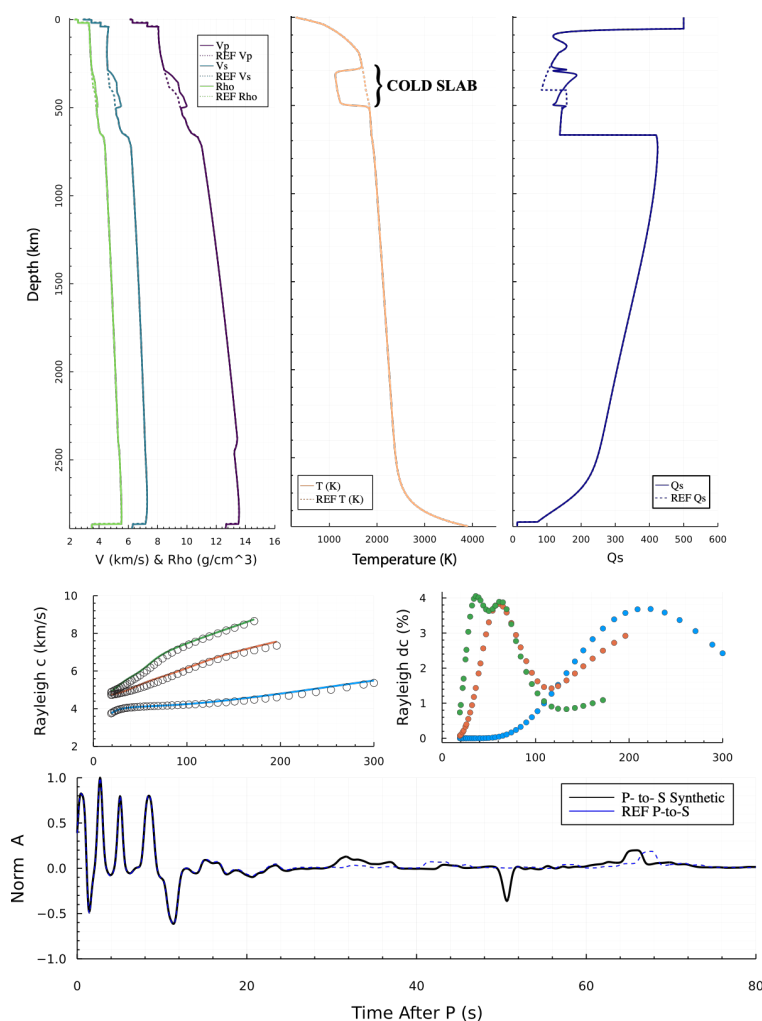
546 **Figure 8: Example 2 showing the effect of a cold slab-like feature plunging into the transition zone. On the top: the left panel**
547 **shows the Vp, Vs and Rho profiles with depth (solid lines are the computed parameters and dashed ones are the PREM values),**
548 **in the center we shows the temperature profile with (T) and without (Ref T), and on the right the attenuation profile with (Qs)**
549 **and without the slab (Qs Ref). On the centre of the figure we present: on the left the dispersion curves of the model with (solid**
550 **lines) and without (circles) the slab for the fundamental mode (blue) and the 1st (orange) and second (green) overtones.**
551 **Anomalies between both are presented in the right panel. At the bottom P-to-S RF with (black) and without (blue) are shown.**
552 **Notice that, except for the first panel, Ref is the reference model without anomalies (see text for details).**

553 **3.3 Example 3: Hot ponding plume head**

554 In the third example (Fig. 9), we implement a thermal and compositional anomaly with respect to the reference model

555 representing a 1D section of a hot horizontally flowing or ponding plume head (wide horizontal zones that extend from

556 the vertical plume conduit at discontinuities; e.g., Dongmo Wamba et al., 2023). The "plume" is the anomaly, which is

557 defined from 600 km to 900 km depth (Fig. 15) and is characterized by: (a) a +600 K thermal anomaly with respect to the

558 ambient mantle; and (b) a chemical anomaly of Al_2O_3 = +0.25 wt% and FeO = +0.5 wt%. The "plume" anomaly shows

559 lower values for the velocities, density, and Qs than the reference model. In this case, the anomalous region is divided

560 into two sections: the upper part (600 km–700 km depth) with extremely low anomalies (caused by melting atop the

561 plume), and the lower part (depth > 700 km) where the decrease in the physical parameters is less pronounced. The

562 temperature and composition anomalies strongly affect synthetic Rayleigh wave dispersion curves. For the long periods

563 in the fundamental mode, and in general for the higher dispersion modes, the phase velocity anomalies are < -5%. The P-

564 to-S receiver function is modified for periods > 40 s as all the lower part of the transition zone is affected by the anomaly,

565 which also generates sharp impedance contrasts. It is worth noting that the effect of the anomaly in this example is so

566 significant that the crustal phases recorded in the receiver functions are slightly affected as well.

567
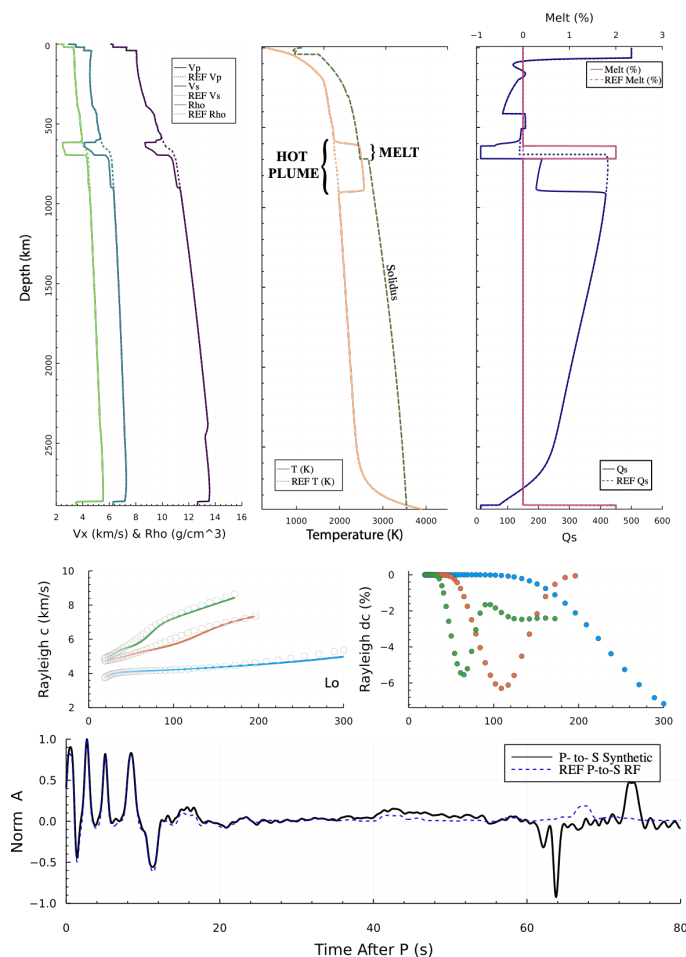
Figure 9: Example 2 showing the effect of a hot plume-like feature entering the transition zone from below. Panels are in the same configuration as in Fig. 8, but in this case we are the melt curve to the top right plot.

3.3 Example 4: Thin Lithosphere

In the final example, we leave most parameters from the reference model constant and change the base of the lithosphere from 200 km in the reference model to 60 km (Fig. 16). This change has a drastic effect on the model as two melt regions appear, one near the LAB and the other at the base of the crust, causing two low velocity, density, and Qs regions at 35 km and 70 km depth, respectively. The effect of the lithospheric thinning is strong in the predicted surface wave dispersion curves, in particular for the fundamental mode, where large negative anomalies are apparent, and less so for the overtones. The waveform of the P-to-S receiver function drastically changes due to the negative impedances present within the crust and upper mantle in our example model. The effect is much less dramatic but still present if the melt modeling option is turned off.
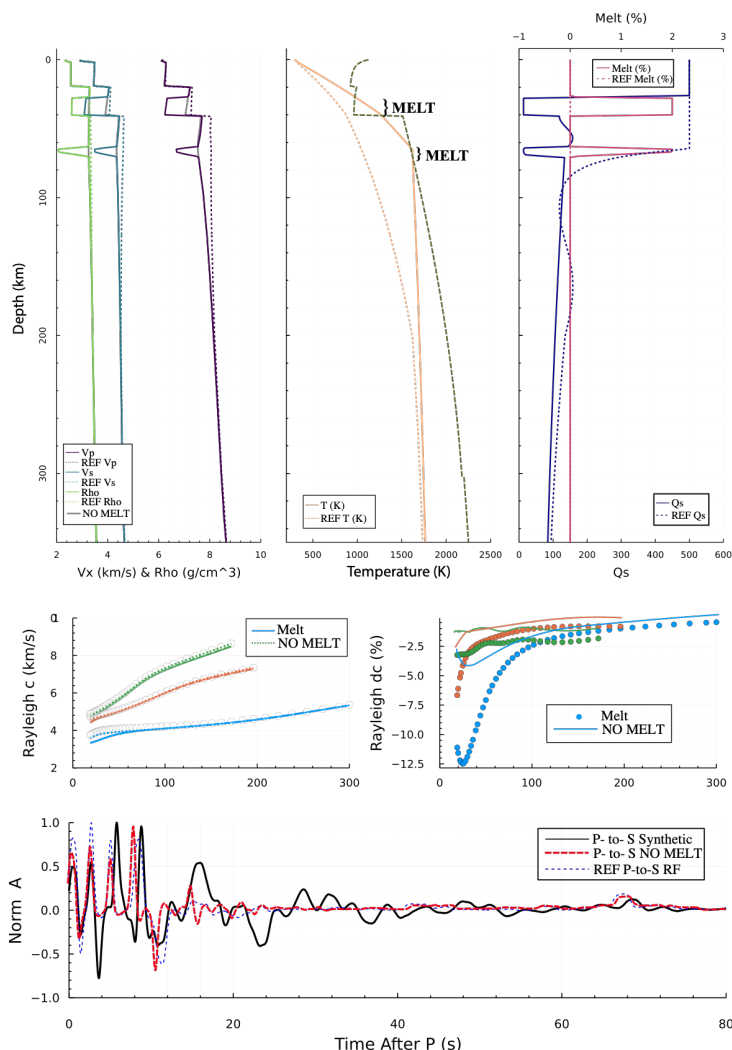
Fig 10 : Example 3 showing the effect of a thin lithosphere under an average continental crust. Panels are the same as in Fig. 8. Here we show two outputs: with melt (MELT, same as in previous examples) and without melt (NO MELT, dotter lines).

4. Remarks, conclusions and further work

Receiver functions and surface wave dispersion data analysis has led to remarkable results revealing the Earth's internal structure in terms of compressional and sheave waves velocity anomalies (δVp, δVs). Yet, the interpretation of these anomalies in terms of crustal and mantle composition is a challenging modelling task. The usage of these data under geophysical-petrological schemes have proven to yield important results in terms of the thermal and petrological structure of the Earth's mantle (e.g. Munch et al., 2018; Bissig et a., 2021; Afonso et al., 2022; Fullea et al., 2021; Munch et al., 2021; Lebedev et al., 2024). Yet, the usage of this type of methods is not common.

597 In order to build a bridge to go from classical seismological approaches to the thermal-petrological realm, we present
598 SEITCOM-1D, a new, open-source, cross-platform, easy-to-use, and accurate code to model the crust and whole mantle
599 using surface wave dispersion curves (including group and phase velocity of Rayleigh and Love waves for the
600 fundamental mode, as well as several overtones) and three widely used receiver functions (P-to-S, S-to-P, and SKS-to-P)
601 directly in terms of rock composition and the in-situ temperature and pressure conditions. We achieved this by creating
602 an interface between the modeling of seismic data and mineral/phase equilibria calculations that allow for the calculation
603 of elastic properties (i.e., Vp, Vs, and density) as a function of temperature, pressure, and composition. Moreover,
604 SEITCOM-1D can be used as a simple geophysical model (i.e., seismic velocities and density) generator based on input
605 thermochemical conditions that can be coupled to third-party seismic codes to perform forward calculations, offering as
606 well a variety of tools intended to interpret geophysical data and models in petrological (e.g., property maps in the $\mathcal{TPC}$
607 space; Fig. 1) and geodynamical terms (e.g. different thermal scenarios, Figs. 14-16).

608 SEITCOM-1D can be used to simultaneously fit different real seismological and other geophysical data sets within a trial-
609 and-error approach or to carry out synthetic modeling (e.g., sensitivity analysis), making it a useful tool for a wide range
610 of geoscientists. Future work includes developing an inversion scheme of seismic data for the thermochemical structure
611 of the crust and mantle based on SEITCOM-1D.

612
613

614
615
616
617
618
619
620
621
622
623
624
625
626
627
628
629
630

631 ***Appendix A: SEITCOM-1D Surface Wave Dispersion native package: SWD.jl***

632   SWD.jl is mostly based in the formulation described by Haney and Tsai (2015, 2017, 2019). These authors utilize (for
633 both Rayleigh and Love waves) a finite element approach based on the thin-layer method (Lysmer, 1970; Kausel, 2005).
634 In contrast to the popular Thomson-Haskell recursion formula (e.g., Takeuchi and Saito, 1972; Saito, 1988), Haney and
635 Tsai employed several thin layers leading to a generalized eigenvalue/eigenvector problem that must be solved for every
636 sampled frequency ($1/T_{Observed}$, Hz). Their method is both accurate and fast and allows for the consideration of a water

637   layer on top of the model column. However, as originally proposed, the method is hampered by two shortcomings: (1) it

638   assumes the Earth is isotropic, elastic and flat, and (2) it requires the specification of a relatively dense Finite Elements

639   (FEM) mesh. We address each one of these as follows:

640

641   (a) We decouple the computation of Rayleigh and Love waves based on the vertically and horizontally polarized

642   $V_S(\mathcal{TPC})$ components, V_{SV} and V_{SH}, respectively defined as:

643
$$V_{SV} = (1 - \frac{1}{3}\chi)V_S \text{ (Eq. A.1)}$$

644
$$V_{SH} = (\frac{2}{3}\chi + 1)V_S \text{ (Eq. A.2)}$$

645   Where χ is the average seismic radial anisotropy for each layer (user input). Rayleigh and Love dispersion curves

646   are computed as a function of V_{SV} and V_{SH} respectively.

647

648   We include anelastic effects as stated by Karato, (1993), Minster and Anderson (1981), Afonso et al. (2005), Fullea et al.

649   (2021), via the expressions:

650
$$V_{Pa} = V_P(1 - \frac{2}{9}cot(\frac{\pi\alpha}{2})Q_s^{-1}) \text{ (Eq. A.3)}$$

651
$$V_{Sa} = V_s(1 - \frac{1}{2}cot(\frac{\pi\alpha}{2})Q_s^{-1}) \text{ (Eq. A.4)}$$

652   Where, V_{Pa} and V_{Sa} are the anelastic P and S velocities, and Vp and Vs are the anharmonic velocities computed from

653   $\mathcal{TPC}$ values. Further details on estimating Qs are presented in section 2.6.

654   (b) We consider the Earth's sphericity correcting the values of Vp, Vs and ρ for the Earth-flattening approximation

655   before computing the dispersion curves. Here, we follow Herrmann (2013) for Rayleigh waves, and the equations

656   by Schwab and Knopoff (1972) for Love waves. The depth from the surface in the equivalent flat Earth model,

657   z, is given by:

658
$$z = a ln\frac{a}{r} \text{ (Eq. A.5)}$$

659   Where r is the radial distance from the center of the Earth, and a is the Earth's radius. Hence, if we consider a

660   spherical layer bounded by r_i and r_{i-1} radii, with $r_{i-1} > r_i$, then the thickness, h, of the corresponding i^{th} flat layer is

661   given by:

662
$$(h_i)_f = a ln(\frac{a}{r_i}) - a ln(\frac{a}{r_{i-1}}) \text{ (Eq. A.6)}$$

663   The mean Vp, Vs and ρ in the transformed flat layer model, $(V_{pi})_f$, $(V_{si})_f$, $(\rho_i)_f$ and are given by

664
$$(Vp_i)_f = (Vp_i)_s \frac{2a}{r_i+r_{i-1}} \text{ (Eq. A.7)}$$

665
$$(Vs_i)_f = (Vs_i)_s \frac{2a}{r_i+r_{i-1}} \text{ (Eq. A.8)}$$

666
$$(\rho_i)_f = (\rho_i)_s \left(\frac{2a}{r_i+r_{i-1}}\right)^{SE} \text{ (Eq. A.9)}$$

667   Where $(V_{pi})_s$, $(V_{si})_s$, $(\rho_i)_s$ are the mean Vp, Vs and ρ in the spherical model, and SE is a parameter that takes a different

668   value for Love (SE=-5, Schwab and Knopoff, 1972) and Rayleigh (we find a better fit with an exponent value of SE=-

669   2.278 instead of SE=-2.275 as originally reported in Herrmann (2013)).

670

671   (c) Finally, we optimize the FEM mesh for the forward computation (e.g., Xia et al., 1999, Ma and Clayton, 2016,

672   Hanney and Tsai, 2015, 2017, 2019). Generally, the required mesh must have adequate sampling above the

673   sensitivity depth of each period, without oversampling the model below it unnecessarily. As a rule of thumb,

674 more than five 5 layers (6 nodes) are required in the sensitivity depths of each frequency with their thicknesses
675 increasing exponentially from the surface to the bottom of the model (e.g., Hanney and Tsai, 2017). In
676 SEITCOM-1D, the user has two possibilities: (i) using a precomputed mesh (the Golden Mesh) created with
677 smaller layers than those required to compute the dispersion at any period between 1 s and 500 s, and slightly
678 oversampling the base of the model; or (ii) using a new mesh based on the lowest period of the input data and a
679 low threshold of Rayleigh wave phase velocity set to 1 km/s (see Hanney and Tsai, 2017, Appendix D for more
680 details). Our mesh samples all the space, and the thickness of each layer coincides with the sensitivity of both
681 Rayleigh waves and Love waves (depending on the period). Our FEM grids for surface waves are designed to
682 compute dispersion curves in the period range from 5 s to 500 s.

683
684
685
686
687
688
689
690
691
692
693
694
695
696
697
698
699
700
701
702
703
704
705
706
707 *Appendix B: seismic attenuation model*
708
709 Dannberg et al (2017) pose that the response of a continuum that behaves according to Burgers model of linear
710 viscoelasticity with creep function in response to a sinusoidally time-varying stress (e.g., a dispersive wave) is given by
711 the dynamic compliance J*(ω) (the Laplace transform of its creep function). This function takes the form:
712 $$J * (\omega) = J_1(\omega) + iJ_2(\omega) \quad \text{(Eq. B1)}$$

713   $$J_1 = J_u \left\{ 1 + \frac{\alpha \Delta_B}{\tau_H{}^\alpha - \tau_L{}^\alpha} \int_{\tau_L}^{\tau_H} \frac{\tau^{\alpha-1}}{1+\omega^2} d\tau + \frac{\Delta_P}{\sigma\sqrt{2\pi}} \int_0^\infty \frac{1}{\tau(1+\omega^2\tau^2)} exp\left(-\frac{ln(\frac{\tau}{\tau_P})^2}{2\sigma^2}\right) d\tau \right\} \text{ (Eq. B2)}$$

714   $$J_2 = J_u \left\{ \frac{\omega\alpha\Delta_B}{\tau_H^\alpha - \tau_L^\alpha} \int_{\tau_L}^{\tau_H} \frac{\tau^\alpha}{1+\omega^2\tau^2} d\tau + \frac{\omega\Delta_P}{\sigma\sqrt{2\pi}} \int_0^\infty \frac{1}{1+\omega^2\tau^2} exp\left(-\frac{ln(\frac{\tau}{\tau_P})^2}{2\sigma^2}\right) d\tau + \frac{1}{\omega\tau_M} \right\} \text{ (Eq. B3)}$$

715   Where ω is the angular frequency, $\omega = 2\pi/T$, α is the anelastic frequency exponent, ΔB is the Burgers element strength

716   and Δ_P and σ are the peak height and width, and Ju is the unrelaxed compliance (which is not computed for Q_s

717   estimations).

718   All the timescales τ_i control the temperature, pressure, and grain size sensitivity of the anelastic scaling relationships:

719

720   $$\tau_i = \tau_{iR}\left(\frac{d}{d_R}\right)^{mi} exp\left[\left(\frac{E^*}{R}\right)\left(\frac{1}{T} - \frac{1}{T_R}\right) + \left(\frac{V^*}{R}\right)\left(\frac{P}{T} - \frac{P_R}{T_R}\right)\right] \text{ (Eq. B4)}$$

721   where $i = H, L, P, M$ are the upper, lower, peak and Maxwell viscous relaxation values respectively, and all m_j are grain

722   size exponents with $j=H, L, P$ for anelastic relaxation (m_a) , and $j=M$ for viscous relaxation (m_v). Here, E^* and V^* are the

723   activation energy and volume for the anelastic model. We use the same values for each major mantle zone as reported in

724   the supplementary material of Dannberg et al. (2017). The temperature, pressure, and grain size sensitivity of the anelastic

725   relationships are introduced in terms of reference values T_R, P_R and d_R.

726   $$Q_s = \frac{J_1(\omega)}{J_2(\omega)} \text{ (Eq. B5)}$$

727   and

728   $$Q_p = \frac{9}{4}Q_s \text{ (Eq. B 6)}$$

729   which implicates an infinite quality factor for the bulk modulus (e.g., Karato, 1993; Minster and Anderson, 1981).

730

731

732

733

734

735

736

737

738

739

740

741   **Acknowledgements**

742

746   **Data Availability Statement**

747

748   The full SeitComp-1D V 1.0 package is available for download from https://github.com/marianoarnaiz/SeitComp.jl or by

749   contacting the corresponding author (mararnai@ucm.es). Fully operating Julia Language (V 1.7 or higher) is required to

750   run the code and the full package has a size of ~64 mb.

751   **Author contribution statement:**

752

753   MA and JF co-designed the algorithms, and co-wrote the manuscript. MA wrote the code in Julia language. JF supervised

754   the research project and tested the code.

755

756

757

758

759

760

761

762

763

764

765

766

767

768

769

770

771

772

773

774

775

776

777

778

779

780

781

782

783

784

785

786   **References**

787   Abers, G. A. and Hacker, B. R.: A MATLAB toolbox and Excel workbook for calculating the densities, seismic wave

788   speeds, and major element composition of minerals and rocks at pressure and temperature, Geochem. Geophys.

789   Geosyst., 16, 616–624, https://doi.org/10.1002/2015GC006091, 2016.

790   Afonso, J. C., Ranalli, G., and Fernández, M.: Thermal expansivity and elastic properties of the lithospheric mantle:

791   results from mineral physics of composites, Phys. Earth Planet. Int., 149, 279–306,

792   https://doi.org/10.1016/j.pepi.2004.09.008, 2005.

793   Aki, K., Christoffersson, A., and Husebye, E. S.: Determination of the 3-dimensional seismic structure of the

794   lithosphere, J. Geophys. Res., 82, 277–296, https://doi.org/10.1029/JB082i002p00277, 1977.

795   Andrault, D., Pesce, G., Manthilake, G., Monteux, J., Bolfan-Casanova, N., Chantel, J., Novella, D., Guignot, N., King,

796   A., Itié, J.-P., and Hennet, L.: Deep and persistent melt layer in the Archaean mantle, Nat. Geosci., 11, 139–143,

797   https://doi.org/10.1038/s41561-017-0053-9, 2018.

798   Arnaiz-Rodríguez, M. S., Zhao, Y., Sánchez-Gamboa, A. K., and Audemard, F.: Crustal and upper-mantle structure of

799   the Eastern Caribbean and Northern Venezuela from passive Rayleigh wave tomography, Tectonophysics, 804, 228711,

800   https://doi.org/10.1016/j.tecto.2020.228711, 2020.

801   Athy, L. F.: Density, porosity and compaction of sedimentary rocks, AAPG Bull., 14, 1–24,

802   https://doi.org/10.1306/3D9322C5-16B1-11D7-8645000102C1865D, 1930.

803   Audhkhasi, P. and Singh, S. C.: Discovery of distinct lithosphere-asthenosphere boundary and the Gutenberg

804   discontinuity in the Atlantic Ocean, Sci. Adv., 8, eabn5404, https://doi.org/10.1126/sciadv.abn5404, 2022.

805   Ball, P. W., White, N. J., Maclennan, J., et al.: Global influence of mantle temperature and plate thickness on intraplate

806   volcanism, Nat. Commun., 12, 2045, https://doi.org/10.1038/s41467-021-22323-9, 2021.

807   Bezanson, J., Edelman, A., Karpinski, S., and Shah, V. B.: Julia: A Fresh Approach to Numerical Computing, SIAM

808   Rev., 59, 65–98, https://doi.org/10.1137/141000671, 2017.

809   Bissell, H. J., Haaf, E. T., Crook, K. A. W., Beck, K. C., Schwab, F. L., and Folk, R. L.: Sedimentary rocks,

810   Encyclopædia Britannica, https://www.britannica.com/science/sedimentary-rock, accessed 9 Dec 2021.

811   Bissig, F., Khan, A., Tauzin, B., Sossi, P. A., Münch, F. D., and Giardini, D.: Multifrequency inversion of Ps and Sp

812   receiver functions: methodology and application to USArray data, J. Geophys. Res. Solid Earth, 126, e2020JB020350,

813   https://doi.org/10.1029/2020JB020350, 2021.

814   Bosch, M.: Lithologic tomography: from plural geophysical data to lithology estimation, J. Geophys. Res., 104, 749–

815   766, https://doi.org/10.1029/1998JB900035, 1999.

816   Boujibar, A., Bolfan-Casanova, N., Andrault, D., Bouhifd, M. A., and Trcera, N.: Incorporation of Fe^{2+} and Fe^{3+} in

817   bridgmanite during magma ocean crystallization, Am. Mineral., 101, 1560–1570, https://doi.org/10.2138/am-2016-

818   5561, 2016.

819   Brocher, T. M.: Empirical relations between elastic wavespeeds and density in the Earth's crust, Bull. Seismol. Soc.

820   Am., 95, 2081–2092, https://doi.org/10.1785/0120040090, 2005.

821   Calò, M., Bodin, T., and Romanowicz, B.: Layered structure in the upper mantle across North America from joint

822   inversion of long and short period seismic data, Earth Planet. Sci. Lett., 449, 164–175,

823   https://doi.org/10.1016/j.epsl.2016.05.054, 2016.

824   Chen, X., Park, J., and Levin, V.: Anisotropic layering and seismic body waves: deformation gradients, initial

825   S-polarizations, and converted-wave birefringence, Pure Appl. Geophys., 178, 2001–2023,

826   https://doi.org/10.1007/s00024-021-02755-6, 2021.

827   Connolly, J. A. D.: Computation of phase equilibria by linear programming: a tool for geodynamic modeling and its

828   application to subduction zone decarbonation, Earth Planet. Sci. Lett., 236, 524–541,

829   https://doi.org/10.1016/j.epsl.2005.03.039, 2005.

830   Connolly, J. A. D.: The geodynamic equation of state: What and how, Geochem. Geophys. Geosyst., 10, Q10014,

831   https://doi.org/10.1029/2009GC002540, 2009.

832   Dinari, O., Yu, A., Freifeld, O., and Fisher, J.: Distributed MCMC inference in Dirichlet process mixture models using

833   Julia, in Proc. IEEE/ACM CCGrid, 518–525, https://doi.org/10.1109/CCGRID.2019.00066, 2019.

834   Dongmo Wamba, M., Montagner, J.-P., and Romanowicz, B.: Imaging deep-mantle plumbing beneath La Réunion and

835   Comores hot spots: vertical plume conduits and horizontal ponding zones, Sci. Adv., 9, eade3723,

836   https://doi.org/10.1126/sciadv.ade3723, 2023.

837   Faul, U. H. and Jackson, I.: The seismological signature of temperature and grain size variations in the upper mantle,

838   Earth Planet. Sci. Lett., 234, 119–134, https://doi.org/10.1016/j.epsl.2005.02.030, 2005.

839   Fullea, J., Afonso, J. C., Connolly, J. A. D., Fernández, M., García-Castellanos, D., and Zeyen, H.: LitMod3D: an

840   interactive 3-D software to model the thermal, compositional, density, seismological, and rheological structure of the

841   lithosphere and sublithospheric upper mantle, Geochem. Geophys. Geosyst., 10, Q08019,

842   https://doi.org/10.1029/2009GC002391, 2009.

843   Fullea, J., Lebedev, S., Martinec, Z., and Celli, N. L.: WINTERC-G: mapping the upper mantle thermochemical

844   heterogeneity from coupled geophysical–petrological inversion of seismic waveforms, heat flow, surface elevation and

845   gravity satellite data, Geophys. J. Int., 226, 146–191, https://doi.org/10.1093/gji/ggab094, 2021.

846   Fukao, Y., Obayashi, M., and Nakakuki, T.: Stagnant slab: a review, Annu. Rev. Earth Planet. Sci., 37, 19–46,

847   https://doi.org/10.1146/annurev.earth.36.031207.124224, 2009.

848   Gao, K., Mei, G., Piccialli, F., Cuomo, S., Tu, J., and Huo, Z.: Julia language in machine learning: algorithms,

849   applications, and open issues, Comput. Sci. Rev., 37, 100254, https://doi.org/10.1016/j.cosrev.2020.100254, 2020.

850   Gerya, T.: Introduction to Numerical Geodynamic Modelling, Cambridge University Press, Cambridge, pp. 345,

851   https://doi.org/10.1017/CBO9780511809101, 2009.

852   Grand, S. P.: Mantle shear-wave tomography and the fate of subducted slabs, Philos. Trans. R. Soc. Lond. A, 360,

853   2475–2491, https://doi.org/10.1098/rsta.2002.1023, 2002.

854   Grose, C. J. and Afonso, J. C.: Chemical disequilibria, lithospheric thickness, and the source of ocean island basalts, J.
855   Petrol., 60, 755–790, https://doi.org/10.1093/petrology/egz012, 2019.

856   Hacker, B. R. and Abers, G. A.: Subduction Factory 3: an Excel worksheet and macro for calculating the densities,
857   seismic wave speeds, and H_2O contents of minerals and rocks at pressure and temperature, Geochem. Geophys.
858   Geosyst., 5, Q01005, https://doi.org/10.1029/2003GC000649, 2004.

859   Hamblin, W. K. and Christiansen, E. H.: Earth's dynamic systems, 10th edn., Prentice Hall, Upper Saddle River, NJ,
860   790 pp., 2004.

861   Haney, M. M. and Tsai, V. C.: Nonperturbational surface-wave inversion: a Dix-type relation for surface waves,
862   Geophysics, 80, EN167–EN177, https://doi.org/10.1190/geo2014-0208.1, 2015.

863   Haney, M. M. and Tsai, V. C.: Perturbational and nonpeturbational inversion of Rayleigh-wave velocities, Geophysics,
864   82, F15–F28, https://doi.org/10.1190/GEO2016-0542.1, 2017.

865   Haney, M. M. and Tsai, V. C.: Perturbational and nonperturbational inversion of Love-wave velocities, Geophysics, 85,
866   F19–F26, https://doi.org/10.1190/geo2019-0058.1, 2019.

867   Haskell, N. A.: The dispersion of surface waves on multilayered media, Bull. Seismol. Soc. Am., 43, 17–34, 1953.

868   Herrmann, R. B.: Computer programs in seismology: an evolving tool for instruction and research, Seism. Res. Lett.,
869   84, 1081–1088, https://doi.org/10.1785/0220110096, 2013.

870   Hofmeister, A. M.: Mantle values of thermal conductivity and the geotherm from phonon lifetimes, Science, 283, 1699–
871   1706, https://doi.org/10.1126/science.283.5409.1699, 1999.

872   Irifune, T. and Tsuchiya, T.: Phase transitions and mineralogy of the lower mantle, in Treatise on Geophysics, Elsevier,
873   pp. 33–60, https://doi.org/10.1016/B978-0-444-53802-4.00030-0, 2015.

874   Irifune, T.: Composition and structure of the Earth's mantle: a view from recent high-pressure mineral physics studies,
875   J. Mineral. Soc. Japan, 19, 233–243, 1990.

876   Jackson, I., Fitz Gerald, J. D., Faul, U. H., and Tan, B. H.: Grain-size-sensitive seismic wave attenuation in
877   polycrystalline olivine, J. Geophys. Res., 107, 2360, https://doi.org/10.1029/2001JB001225, 2002.

878   Julià, J., Ammon, C. J., Herrmann, R. B., and Correig, A. M.: Joint inversion of receiver function and surface wave
879   dispersion observations, Geophys. J. Int., 143, 99–112, https://doi.org/10.1046/j.1365-246X.2000.00217.x, 2000.

880   Karato, S.-i. and Wu, P.: Rheology of the upper mantle: a synthesis, Science, 260, 771–778,
881   https://doi.org/10.1126/science.260.5109.771, 1993.

882   Kausel, E. Some wave propagation modes from simple systems to layered soils, in Lai, C. G., and Wilmanski, K. (eds.),
883   *Surface waves in geomechanics: direct and inverse modeling for soil and rocks*, Springer-Verlag, 165–202, 2005.

884   Kennett, B. L. N.: Seismic wave propagation in stratified media, ANU Press, https://doi.org/10.2307/j.ctt24h2zr, 2009.

885   Kennett, B. L. N. and Engdahl, E. R.: Travel times for global earthquake location and phase association, Geophys. J.
886   Int., 105, 429–465, https://doi.org/10.1111/j.1365-246X.1991.tb06724.x, 1991.

887   Haney, M. M. and Tsai, V. C.: Perturbational and nonperturbational inversion of Love-wave velocities, Geophysics, 85,
888   F19–F26, https://doi.org/10.1190/geo2019-0164.1, 2020.

889   Huang, Z., Zhao, D., and Wang, L.: Seismic heterogeneity and mantle dynamics of the western Pacific subduction zone,
890   J. Geophys. Res. Solid Earth, 116, B10303, https://doi.org/10.1029/2011JB008401, 2011.

891   Irifune, T., Isshiki, M., and Katayama, Y.: Iron partitioning and density changes of pyrolite in Earth's lower mantle,
892   Science, 292, 1171–1173, https://doi.org/10.1126/science.1057647, 2001.

893   Jackson, I. and Faul, U. H.: Grainsize-sensitive viscoelastic relaxation in olivine: towards a robust laboratory-based
894   model for seismological application, Phys. Earth Planet. Int., 183, 151–163, https://doi.org/10.1016/j.pepi.2010.09.005,
895   2010.

896   Jackson, M. G. and Dasgupta, R.: Compositional constraints on melting of Earth's heterogeneous mantle and
897   implications for the generation of ocean island basalts, Rev. Geophys., 56, 3–49,
898   https://doi.org/10.1002/2017RG000558, 2018.

899   Karato, S.: On the origin of the asthenosphere, Earth Planet. Sci. Lett., 321–322, 95–103,
900   https://doi.org/10.1016/j.epsl.2012.01.001, 2012.

901   Kellogg, L. H., Hager, B. H., and van der Hilst, R. D.: Compositional stratification in the deep mantle, Science, 283,
902   1881–1884, https://doi.org/10.1126/science.283.5409.1881, 1999.

903   Khan, A., Maclennan, J., and Connolly, J. A. D.: Inversion of seismic and geodetic data for the major element chemistry
904   and temperature of the Earth's mantle, Earth Planet. Sci. Lett., 284, 554–568,
905   https://doi.org/10.1016/j.epsl.2009.05.014, 2009.

906   Khan, A., Cammarano, F., and Connolly, J. A. D.: Geophysical evidence for melt in the deep mantle, Nature, 455, 978–
907   981, https://doi.org/10.1038/nature07364, 2008.

908   Kustowski, B., Ekström, G., and Dziewoński, A. M.: Anisotropic shear-wave velocity structure of the Earth's mantle: a
909   global model, J. Geophys. Res., 113, B06306, https://doi.org/10.1029/2007JB005169, 2008.

910   Lebedev, S. and van der Hilst, R. D.: Global upper-mantle tomography with the automated multimode inversion of
911   surface and S-wave forms, Geophys. J. Int., 173, 505–518, https://doi.org/10.1111/j.1365-246X.2008.03721.x, 2008.

912   Lekic, V., Cottaar, S., Dziewoński, A., and Romanowicz, B.: Cluster analysis of global lower mantle tomography: a
913   new class of structure and implications for chemical heterogeneity, Earth Planet. Sci. Lett., 357–358, 68–77,
914   https://doi.org/10.1016/j.epsl.2012.09.014, 2012.

915   Matas, J., Bass, J. D., Ricard, Y., Mattern, E., and Bukowinski, M. S. T.: On the bulk composition of the lower mantle:
916   predictions and limitations from generalized inversion of radial seismic profiles, Geophys. J. Int., 160, 973–990,
917   https://doi.org/10.1111/j.1365-246X.2005.02526.x, 2005.

918 Montagner, J. P. and Kennett, B. L. N.: How to reconcile body-wave and normal-mode reference Earth models,
919 Geophys. J. Int., 125, 229–248, https://doi.org/10.1111/j.1365-246X.1996.tb06548.x, 1996.

920 Murakami, M., Hirose, K., Kawamura, K., Sata, N., and Ohishi, Y.: Post-perovskite phase transition in MgSiO$_3$,
921 Science, 304, 855–858, https://doi.org/10.1126/science.1095932, 2004.

922 Nolet, G., Montelli, R., Dahlen, F. A., Masters, G., Engdahl, E. R., and Hung, S. H.: Seismic evidence for a deep mantle
923 thermal anomaly in the mantle beneath East Africa, Geophys. Res. Lett., 31, L20607,
924 https://doi.org/10.1029/2004GL020572, 2004.

925 Ritsema, J., Deuss, A., van Heijst, H. J., and Woodhouse, J. H.: S40RTS: a degree-40 shear-velocity model for the
926 mantle from new Rayleigh wave dispersion, teleseismic traveltime and normal-mode splitting function measurements,
927 Geophys. J. Int., 184, 1223–1236, https://doi.org/10.1111/j.1365-246X.2010.04884.x, 2011.

928 Rudolph, M. L., Lekic, V., and Lithgow-Bertelloni, C.: Viscosity jump in Earth's mid-mantle, Science, 350, 1349–
929 1352, https://doi.org/10.1126/science.aad1929, 2015.

930 Simmons, N. A., Forte, A. M., and Grand, S. P.: Thermochemical structure and dynamics of the African superplume,
931 Geophys. Res. Lett., 34, L02301, https://doi.org/10.1029/2006GL028009, 2007.

932 Stixrude, L. and Lithgow-Bertelloni, C.: Thermodynamics of mantle minerals – I. Physical properties, Geophys. J. Int.,
933 162, 610–632, https://doi.org/10.1111/j.1365-246X.2005.02642.x, 2005.

934 Stixrude, L. and Lithgow-Bertelloni, C.: Thermodynamics of mantle minerals – II. Phase equilibria, Geophys. J. Int.,
935 184, 1180–1213, https://doi.org/10.1111/j.1365-246X.2010.04890.x, 2011.

936 Takei, Y.: Effect of pore geometry on Vp/Vs: From equilibrium geometry to crack, J. Geophys. Res. Solid Earth, 107,
937 ECV 6-1–ECV 6-12, https://doi.org/10.1029/2001JB000522, 2002.

938 Tsuchiya, T., Tsuchiya, J., Umemoto, K., and Wentzcovitch, R. M.: Phase transition in MgSiO$_3$ perovskite in the
939 Earth's lower mantle, Earth Planet. Sci. Lett., 224, 241–248, https://doi.org/10.1016/j.epsl.2004.05.017, 2004.

940 van der Hilst, R. D., Widiyantoro, S., and Engdahl, E. R.: Evidence for deep mantle circulation from global
941 tomography, Nature, 386, 578–584, https://doi.org/10.1038/386578a0, 1997.

942 Walter, M. J., Kohn, S. C., Araujo, D., Bulanova, G. P., Smith, C. B., Gaillou, E., Wang, J., Steele, A., and Shirey, S. B.:
943 Deep mantle cycling of oceanic crust: evidence from diamonds and their mineral inclusions, Science, 334, 54–57,
944 https://doi.org/10.1126/science.1209300, 2011.